International Journal of Rotating Machinery, 8(2): 125–140, 2002

1023-621X/02 $12.00 + .00

Turbulent Flow and Endwall Heat Transfer Analysis in a 90° Turning Duct and Comparisons with Measured Data

Part II: Influence of Secondary Flow, Vorticity, Turbulent Kinetic Energy, and Thermal Boundary Conditions on Endwall Heat Transfer

KUISOON KIM*, BRIAN G. WIEDNER†, and CENGIZ CAMCI‡
Turbomachinery Heat Transfer Laboratory, Department of Aerospace Engineering, The Pennsylvania State University, University Park, Pennsylvania 16802, USA

Fundamental character of forced convection heat transfer to the endwall surface of a gas turbine passage can be simulated by using a 90° turning duct. Elevated operating temperatures in gas turbines require a thorough understanding of the turbulent thermal transport process in the three-dimensional end-wall boundary layers. The current study uses an in-house developed three-dimensional viscous flow solver to computationally investigate the heat transfer character near the endwall surfaces. Extensive heat transfer experiments also illuminate the local heat transfer features near the endwall surface and form a baseline data set to evaluate the computational method used. Present experimental effort at $Re = 342{,}190$ employs a prescribed heat flux method to measure convective heat transfer coefficients on the end-wall surface. Local wall temperatures are measured with liquid crystal thermography.

Local convective heat flux is determined by solving the electric potential equation with constant uniform potential that is applied along the inlet and exit boundaries of the endwall. The viscous flow and heat transfer computation algorithms are based on the same methods presented in Part I. The influence of the two primary counter-rotating vortices developing as a result of the balance of inertia and pressure forces on the measured and computed endwall heat transfer coefficients is demonstrated. It is shown that the local heat transfer on the endwall surface is closely related to the structure of the three-dimensional mean flow and the associated turbulent flow field. A comparison of the molecular/turbulent heat diffusion, wall shear stress, visualization of local turbulent kinetic energy are a few of the tasks that can be performed using a numerical approach in a relatively time efficient manner. The current numerical approach is capable of visualizing the near wall features that can not be easily measured in the flow field near the end-wall surfaces.

Keywords: Turbomachinery; Ducts; Fluid mechanics; Heat transfer; Numerical analysis; Experimental aerodynamics; Liquid crystal thermography

During the past few decades cycle maximum temperatures imposed in thermal turbomachinery increased continuously. Elevated temperature operation enables many gas turbine systems to operate at higher cycle efficiency with reduced fuel consumption. Improvements in specific power due to higher temperature operation also result in more geometrically compact systems. There is a tremendous need to predict local heat transfer coefficients accurately in flow passages used in high temperature thermal systems. Improving the quality of these predictive schemes requires

Received 16 June 2000; In final form 30 June 2000.
The experimental study in the turning duct was completed by Dr. B. G. Wiedner. The authors would like to acknowledge the initial efforts of Dr. Tiengli Wang for running the Navier–Stokes solver originally developed by Dr. Kuisoon Kim. The authors acknowledge the continuous support of S. A. Hippensteele of NASA Lewis Research Center for the experimental part of this investigation.
*Present address: Pusan National University, Dept. of Aerospace Engineering, Pusan, Korea. E-mail: Kuskim@hyowon.pusan.ac.kr
†Present address: Brown and Root Energy Services, Texas, USA. E-mail: Brian.Wiedner@halliburton.com
‡Corresponding author. Fax: 814 865 7092. E-mail: C-Camci@psu.edu

high quality fluid mechanics and heat transfer data from carefully executed experiments. The current study is a detailed assessment of a general computational heat transfer method that can be used in the prediction of heat transfer rates in thermal turbomachinery. Numerical heat transfer performance of the method is tested against measured data. The turning duct effectively simulates the streamwise acceleration characteristics, passage vortices and endwall boundary layers of a turbomachinery passage. The turning duct is also an ideal environment to obtain fluid mechanics/heat transfer data with high accuracy and resolution in a controlled laboratory environment.

In thermal turbomachinery applications, a variation in heat transfer rate due to a small flow disturbance can lead to an increase in thermal stress and a decrease in component life. This is true for both hot gas side and coolant side of turbomachinery passages. On a highly curved wall, the change in heat transfer rate is mainly due to an increase or decrease of the turbulent mixing by the effect of the streamline curvature. It has been indicated in von Karman's stability argument (1934) that the convex wall has a stabilizing effect on fluid particles, while the concave wall has a de-stabilizing effect with respect to an equivalent reference flat plate. The measurement and prediction of heat transfer rates for a two-dimensional boundary layer on a concave and convex surface have been presented by Mayle et al. (1979). It was found that the heat transfer on the convex surface was less than a flat surface having the same free stream Reynolds number and turbulence. Concave surface heat transfer was augmented when compared to the flat surface. Good agreement between the numerical results and heat transfer experiments was noted for the convex surface when a two-dimensional differential boundary layer code was used with modified curvature model. For the concave surface, the agreement with the measured heat transfer data was poor due to the uncertainties in the turbulence model. Camci (1985) obtained similar conclusions in heat transfer experiments performed on a gas turbine rotor blade under realistic free stream conditions.

Secondary flow in a duct has been generally classified into two categories. Secondary flows of the first kind were derived from the unbalanced body force caused by the change of streamline curvature. Secondary flows of the second kind in a straight duct of rectangular cross-section were observed in early twenties. It was not until the work of Brundrett and Baines (1964); Perkins (1970); and Launder and Ying (1972) that a complete description was provided. From an analysis of the vorticity transport equation in the streamwise direction, they deduced that the secondary velocities were generated by the Reynolds stress gradients in the plane of duct cross-section. Later, Melling and Whitelaw (1976) gave a quantitative description of Reynolds stress, kinetic energy and secondary velocity in the fully developed flow. Although the magnitude of turbulence driven secondary flow motion is only the order of $2-3\%$ of the streamwise mean velocity, the motion causes the streamwise mean velocity and temperature fields to be distorted considerably toward the corners, and it can produce a substantial modification in the heat transfer coefficient. The study of the influence of secondary flow on heat transfer dates back to 1967. Early measurements of heat transfer coefficient and secondary flow were performed in a vertical straight duct. Numerical prediction of this flow with algebraic and anisotropic two-equation turbulent models was performed by Emery et al. (1980) and Myong (1991). Their investigation indicated that the wall shear stress/wall heat flux first arises from the symmetry plane toward the corner, with a peak shear stress/heat flux about midway between the corner and midpoint of the duct sides, and then falls again near the corner, approaching zero at the corner. In a curved duct flow, the major secondary flow is of the first kind secondary flow but little is known about its effect on the heat transfer coefficient. Only a few experimental measurements in this area were performed in the last few decades and the numerical predictions have not appeared in the literature. Mori et al. (1971) presented an analytical and experimental study for a fully developed laminar flow in a 220° square duct with a constant-wall-heat-flux boundary condition. The flow and temperature fields were divided into two regions as the core and boundary layer regions. The analytical results were obtained by considering the balance of kinetic energy and entropy production in the boundary layer. Temperature distributions and local Nusselt numbers on the wall of a 180° bend have been measured by Johnson and Launder (1985). The experimental results at a Reynolds number of 56,030 showed that the ratio of heat transfer coefficient of the concave and convex surface of 90° section was about $2:1$ at mid-span. Other similar measurements for a strongly curved duct flow were documented in Graziani et al. (1980) and Mayle et al. (1979). Recently, a comprehensive description of streamwise mean flow, secondary flow, and endwall heat transfer coefficient in a 90° turning duct was presented by Wiedner (1994) and Wiedner and Camci (1996a, b, 1997). Several distinct regions of the heat transfer coefficient on the endwall were characterized as the result of the interactions between turbulent flow field and endwall thermal boundary layer. The non-uniform endwall heat flux boundary condition was determined accurately by applying electric field theory and a finite element method, Wiedner and Camci (1986a).

At the present time, comparisons between the calculated and measured local endwall heat transfer in a curved duct of square cross-section have not appeared in the open literature. It is the intent of this paper to provide a better understanding of the influence of the secondary flow as well as the local turbulent flow characteristics on the endwall heat transfer coefficient. In the present study, interactions of the vorticity, turbulent kinetic energy, and turbulent shear stress with the endwall heat transfer were investigated. The data for comparison were based on recent measurements in a 90° turning duct by Wiedner and Camci (1997). The accurate endwall thermal boundary condition of non-uniform heat flux was prescribed during the solution of thermal energy. The computational technique used for the solution of the turbulent flow field in Part I is extended to include the thermal energy equation in this paper.

NUMERICAL MODEL AND THERMAL BOUNDARY CONDITIONS

The Energy Equation

For three-dimensional steady, incompressible, turbulent flows, the governing equations and the solution method for the momentum, energy and turbulent kinetic energy equations were described in Part I. Since the flow is assumed incompressible, the energy equation can be de-coupled from the solution procedure. The conservative form of convection-diffusion equation for the energy equation is as follows:

$$\frac{\partial}{\partial x}\left(\rho U_x T - \Gamma_\phi \frac{\partial T}{\partial x}\right) + \frac{\partial}{\partial y}\left(\rho U_y T - \Gamma_\phi \frac{\partial T}{\partial y}\right) + \frac{\partial}{\partial z}\left(\rho U_z T - \Gamma_\phi \frac{\partial T}{\partial z}\right) = 0 \quad [1]$$

where $\Gamma_\phi = (\mu/Pr) + (\mu_t/Pr_t)$. Equation [1] was obtained under the following assumptions: (1) C_p is a constant; (2) the molecular thermal diffusion is modeled with the Fourier's law; (3) the turbulent heat flux is modeled in Boussinesq form; and (4) the dissipation term and pressure gradient are negligible when compared to the convective terms. The laminar and turbulent Prandtl numbers, are chosen to be 0.7 and 0.9 for air respectively. The discretized equation and the solution method for the energy equation are similar to those for the momentum and turbulence equations. The details of the transformations from the Cartesian coordinates (x, y, z) to the generalized coordinates (ξ, η, ζ) were discussed in Part I. Near the wall, the following logarithmic temperature profile of Launder and Spalding (1974) is employed to build the relationship between the wall temperature and the temperature at the first grid point, provided that the first grid point is located in the fully turbulent region.

$$\frac{(T_p - T_w) C_p \rho C_\mu^{1/4} k_p^{1/2}}{q''_w} = \frac{Pr}{\kappa} \ln E y_p^+ + Pr \frac{\pi/4}{\sin \pi/4}\left(\frac{A}{\kappa}\right)^{1/2}\left(\frac{Pr}{Pr_t} - 1\right)\left(\frac{Pr_t}{Pr}\right)^{1/4} \quad [2]$$

where constant E and κ are 9.739 and 0.4187. A is the Van Driest's constant, equal to 26.0. The viscous sub-layer thickness was determined from the condition $y_p^+ = 4$. The energy equation was considered as converged when the sum of the energy flux residuals at all nodes was less than 0.01% of the inlet energy flux. All the computations were performed with $81 \times 49 \times 49$ grid points in the streamwise, vertical, and radial directions to obtain grid independent solutions.

Thermal Boundary Conditions

The geometry of the duct with heated endwall surface is shown in Figure 1. For the unheated walls and the inlet condition, the temperature is set to the ambient temperature; i.e., 298°K. At the exit of the duct, zero temperature gradient in the streamwise direction is prescribed. Prescription of the heat flux field on the top wall requires the solution of an electrostatic boundary value problem described in Wiedner and Camci (1996). The numerically determined wall heat flux distribution on the endwall surface is used as a boundary condition both in computations and experiments. For a two-dimensional, isotropic, homogeneous conducting medium with zero free charge, the electrical potential V must satisfy,

$$\nabla^2 V(x, y) = 0 \quad [3]$$

The electric boundary conditions for the heated surface are uniform potential at the beginning (line AB) and the end (line CD) of the medium along Y direction and zero current flow normal to the unbounded streamwise edges. An electric field vector can be defined as the gradient of the scalar potential field, $V(x, y)$.

$$\vec{E} = -\vec{\nabla} V \quad [4]$$

Once the electric potential and electric field vector are obtained, a scalar multiplication of the electric field and electrical conductivity σ of the medium provide the current density field,

$$\vec{J} = \sigma \vec{E} \quad [5]$$

Finally, the heat flux is determined from

$$q''_{\text{gen}} = \delta \vec{E} \cdot \vec{J} \quad [6]$$

where δ is the thickness of the electrically conducting medium. This general local heat flux formulation allows us

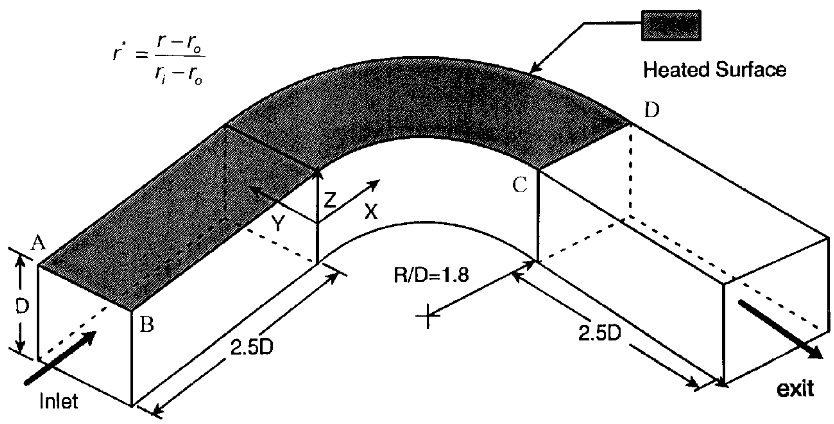

FIGURE 1 90° turning duct geometry, coordinate system, and electrically heated heat transfer surface.

to obtain an accurate thermal endwall boundary condition for the solution of the energy equation.

EXPERIMENTAL AND COMPUTATIONAL RESULTS AND DISCUSSION

Prescribed Heat Flux on the Endwall

The geometry of the 90° turning duct with mean radius to duct width ratio of $(r_i + r_o)/2 = 2.3$ is shown in Figure 1. The top endwall surface shown as the shaded wall was electrically heated by applying DC current to bus bars attached along the inlet line *AB* and exit line *CD*. The rest of the Plexiglas walls were treated as constant temperature surfaces kept at ambient temperature of 298°K. A 5 VDC equi-potential line at the leading edge of the top wall (*AB*) and 0 VDC equi-potential line at $X = 90°$ (*CD*) were used as the prescribed electrical potential boundary conditions. Along the curved inner and outer wall boundaries, no cross-current electrical flow boundary condition was imposed. Electrical current was only allowed to flow tangential to the curved boundaries. The prescribed local heating in the conducting foil that was made of Inconel was computed from Eqs. [3]–[6] by using a finite elements based solver described in Wiedner and Camci (1996b). The endwall heat flux distribution obtained from the numerical solution of the electrostatic boundary value problem is shown in Figure 2. A correction on the generated heat flux was needed due to the conduction and radiation losses from the endwall surface. In the far upstream region, the prescribed heat flux was relatively uniform. The heater foil shape in the inlet section was close to a rectangular shape that has the capability to generate almost uniform local heat flux. The curved section of the duct started at about 2.5 *D* downstream of the inlet section. As soon as the turning section is encountered, an almost elliptic heat flux distribution was observed. The final section of the straight part of the inlet duct was also slightly influenced from the distributions in the curved section because of the elliptic

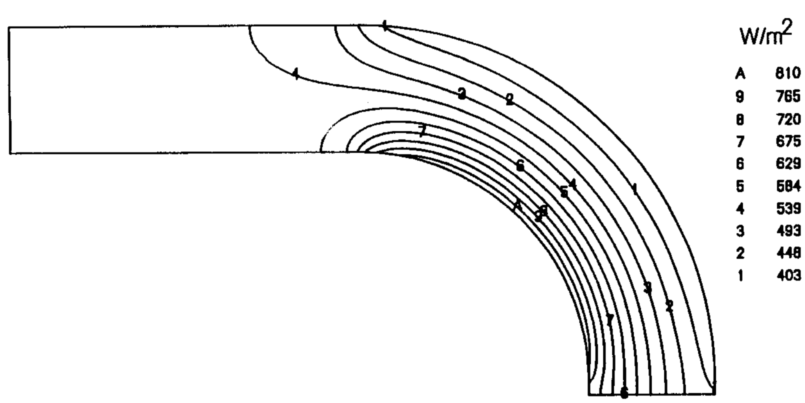

FIGURE 2 Prescribed endwall heat flux distribution (for 5 VDC between bus bars *AB* and *CD*).

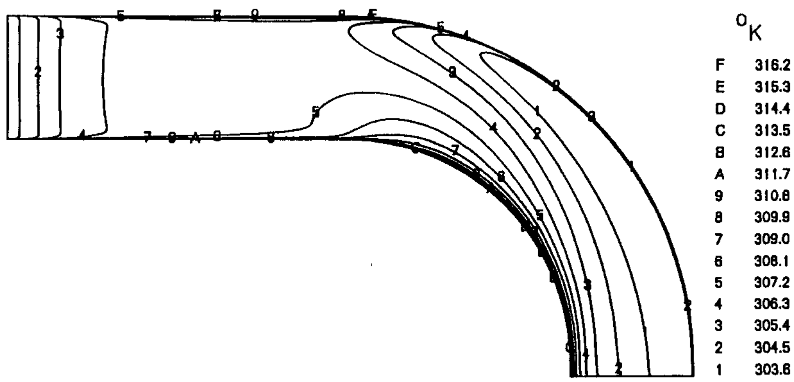

FIGURE 3 Endwall temperature distribution as numerically predicted by thermal energy equation.

nature of electrical potential field. The overall electrical current flow in the thin foil was comparable to the inviscid, irrotational, two-dimensional fluid flow through the endwall surface. The electrical potential $V(x, y)$ corresponded to potential function of the inviscid flow $\phi(x, y)$. The current density field vector was also analogous to the velocity vector. Figure 3 shows the endwall static temperature distribution as numerically calculated from the solution of Eq. [1]. In the entrance region, the endwall showed a continuous temperature increase from 298° to about 307°K within the first duct width (D) distance downstream. Higher temperatures near the convex surface were consistent with the existence of large magnitude current density vectors in this area.

Measurement Uncertainties on Heat Transfer Coefficient *h*

The experimental uncertainty of the convective heat transfer coefficient was estimated according to the procedures given by Kline and McClintock (1953). The uncertainties were $\pm 1\%$ on generated wall heat flux rate (Inconel foil), $\pm 3.4\%$ on wall to free stream temperature difference and $\pm 3.8\%$ on heat transfer coefficient h, based on a 95 percent confidence interval. The uncertainties in the determination of conductive and radiative losses are non-negligible, however their small magnitudes relative to the generated heat flux rate produces only a minor influence in the heat transfer coefficient uncertainty, Wiedner and Camci (1997). High numerical accuracy that can be reached *via* the finite element method used in the prescription of generated heat flux results in reasonably low h uncertainty.

Measured Heat Transfer Coefficients and Comparison with Computations

Figure 4 shows (a) calculated and (b) measured endwall convective heat transfer coefficient h, that is determined according to,

$$h = \frac{q''_{\text{conv}}}{T_w - T_\infty} = \frac{C_{\text{corr}} \times q''_w}{T_w - T_\infty} \qquad [12]$$

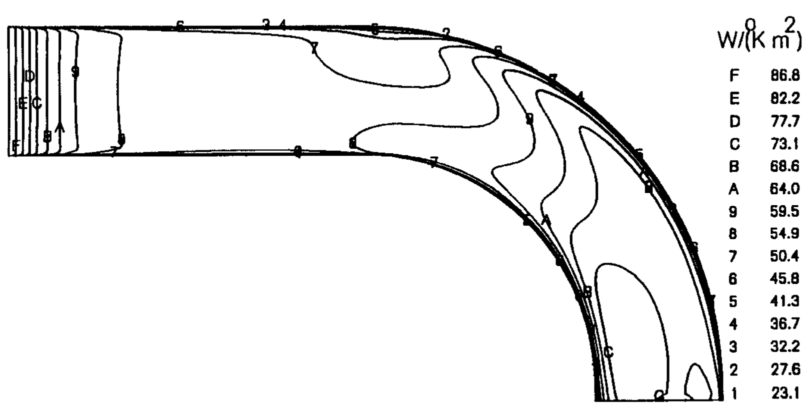

FIGURE 4a Computed end-wall heat transfer coefficient h in [W/m^{2}K].

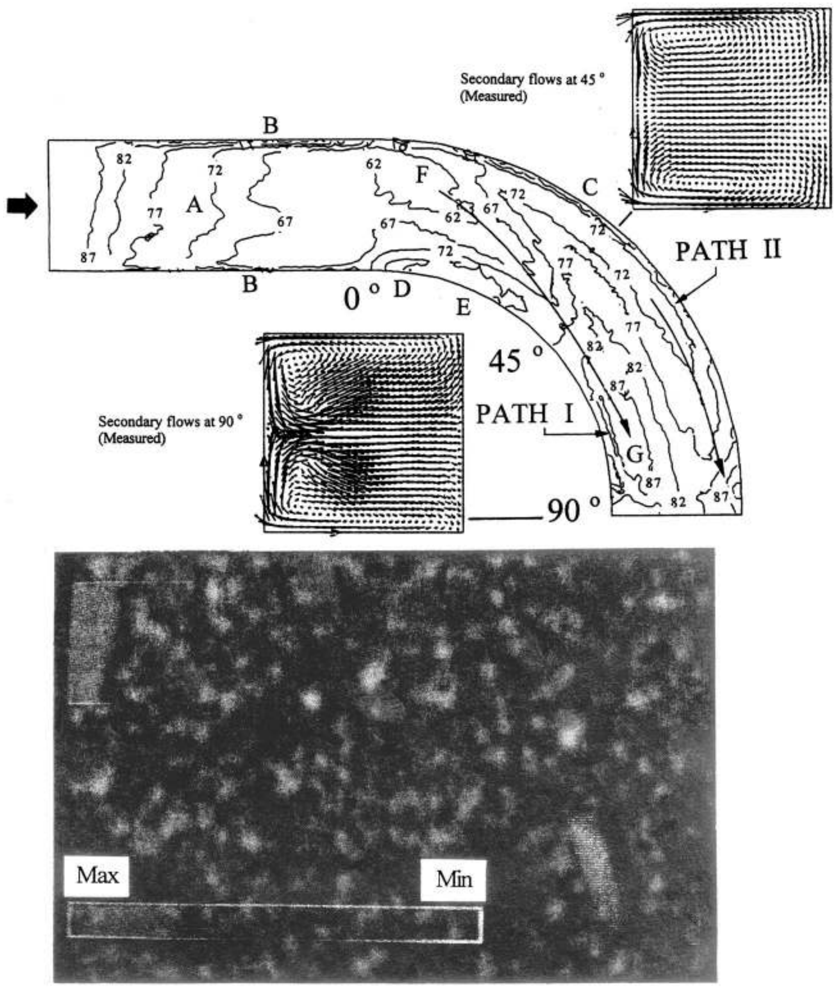

FIGURE 4b Measured end-wall heat transfer coefficient h in [W/m^{2}K] (including measured secondary flow patterns).

C_{corr} is the correction coefficient representing the percentage of generated heat flux removed by forced convection from the endwall surface. (1.0-C_{corr}) indicates the thermal energy loss rate *via* conduction and radiation. Details of the procedure used in the determination of accurate local values of C_{corr} on the endwall surface are given in Wiedner and Camci (1994). The free-stream temperature was fixed at an ambient temperature of 298°K.

Several distinct regions of interest on the endwall have been labeled $A-G$ and Paths I and II, Figure 4b. The entry region (A) prior to the 90° turn shows a streamwise decrease in the heat transfer coefficient from the inlet to the 0° cross section. The streamwise decline in heat transfer coefficient is controlled by the growth of hydrodynamic and thermal boundary layers. Narrow regions of high heat transfer with strong gradients in the cross-stream direction are shown near the inner and outer radius corners (B). Specific corner flows, as described by Brundett and Baines (1964) and Gessner (1973), in these regions may be responsible for higher heat transfer levels. Figure 4b shows that the strong gradient regions of h in the straight inlet section of the duct coincide with the regions that have the highest turbulent velocity fluctuations.

An enhancement in heat transfer (D) followed by a low heat transfer region (E) occurs near the inner radius surface between 0 and 45° cross sections where the initial development of cross stream velocities takes place. Similar patterns were observed in the cascade results of Goldstein and Spores (1988). They attributed the high heat transfer zone to a local highly turbulent flow that resulted from the transverse pressure gradient turning the endwall boundary layer. In regions D and E, shown in Figure 4b, a highly accelerated boundary layer on the convex inner surface and the endwall boundary layer merge together in the corner region. The mean flow in this corner region after the 0° section is highly three-dimensional. The endwall boundary layer fluid starts to develop the secondary velocities in a direction from the concave outer wall to convex inner wall between the 0° and 45° locations. Between the inlet section and the 0° section, the inlet endwall boundary layer on the heat transfer surface is not subject to streamwise curvature. The inlet flow away from the corners has almost a two-dimensional core flow structure as shown in Part I of this paper. Immediately after 0° section, near region D, this structure is somewhat disturbed by the immediate development of centrifugal forces, static pressure gradient in the Y direction, stagnation pressure gradient in the Z direction, and the highly accelerated boundary layer on the inner radius side wall. Region D experiences a locally enhanced mode of turbulent heat transport ($77-82\,\mathrm{W/m^2K}$) due to its highly strained mean flow structure. Immediately downstream of region D, a relatively reduced heat transfer coefficient island (E) ($67-72\,\mathrm{W/m^2K}$) exists. Turbulent momentum and heat exchange in this region may be reduced due to further acceleration of the fluid near the inner radius wall between the 20° and 45° cross sections.

At the 0° cross section, a gradient in the heat transfer coefficient exists with higher levels near the inner radius surface and lower levels near the outer radius surface (F). The favorable and adverse pressure gradients near the inner and outer surfaces, respectively, resulted in accelerated heat transfer level (Path I). This path forms the characteristic wedge shape that has been described by Graziani et al. (1980) and can also be seen in the cascade results of Gaugler and Russell (1984); Goldstein and Spores (1988); and Boyle and Russel (1989). The path crosses the 45° cross section at an approximate value of $Y/D = 0.25$. Detailed flow data shows that the highest secondary velocity vectors adjacent to the endwall occur at this position. Similar circumstances are apparent at the 90° cross section. Although the streamwise component of the mean velocity is relatively reduced in the core (G) of the passage vortices, the related local turbulence enhancement due to enhanced levels of secondary kinetic energy produces relatively high convective heat transfer levels comparable to the inlet section.

Traversing the endwall radially inward, a decrease in the heat transfer coefficient occurs as the inner radius surface and endwall corner is approached. This decrease in heat transfer may be the result of the secondary velocity reduction followed by the abrupt turning of the flow onto the inner radius surface. The secondary flow conditions are similar to those present in a longitudinal vortex. Eibeck and Eaton (1987) showed a decrease in the Stanton number on the up-wash side of the vortex.

Finally in the outer radius region of the passage endwall between the 45° and 90° cross sections, the streamwise pressure gradient changes from adverse to favorable. This pressure gradient reversal results in an acceleration of the streamwise velocity. The endwall heat transfer coefficient distribution in this region indicates a path of increasing heat transfer that continues through the 90° cross section, Path II. The elevated heat transfer coefficient values ($87-92\,\mathrm{W/m2K}$) measured near the outer surface corner at the 90° section lie in this path of increasing heat transfer.

y^+ Distribution Near the Endwall Surface

The viscous sub-layer in the present computations was defined as the fluid layers that occupied the region where $y^+ \leq 4$. Figure 5 is a plot of non-dimensional distance $y^+ = \sqrt{\tau_w/\rho} \cdot y/\nu$ for the first two planes parallel to the endwall (Y, Z plane) passing from the first three grid points. In the plane passing from the first grid point, all contour lines indicated that the viscous sub-layer is below the first grid point. The minimum observed y^+ value was always greater than 7 in the first plane. The highest y^+ values were encountered in the region where passage vortex clearly affects the endwall heat transfer. This region as surrounded by contour line D, contained the highest wall shear stress magnitudes. Similar qualitative trends were observed in the plane passing from the second grid point.

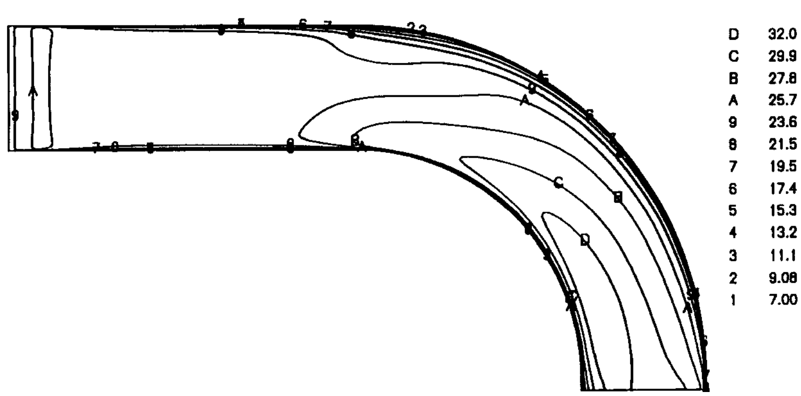

FIGURE 5a y_p^+ of the first grid point away from top wall.

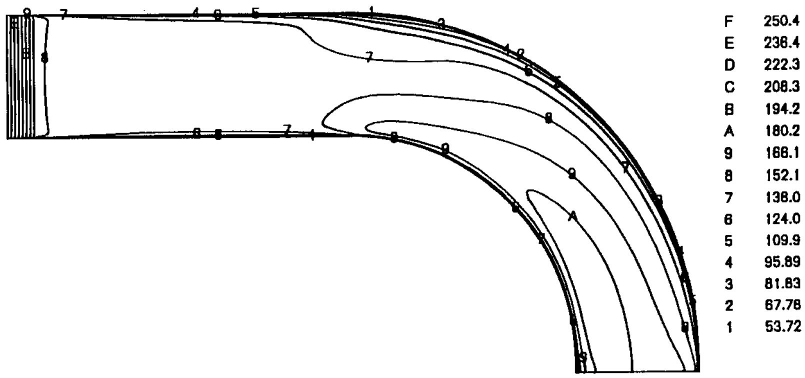

FIGURE 5b y_p^+ of the second grid point away from top wall.

Relationship Between Calculated Turbulent Kinetic Energy and Mean Vorticity and Heat Transfer Coefficient

Figure 6 shows the distribution of predicted TKE on the endwall surface from the computational model discussed previously. Turbulent kinetic energy is plotted in three horizontal planes passing from the first second and third grid points in the domain. There is a strong similarity between the measured/computed heat transfer contours and the computed TKE distribution near the endwall surface. The computational simulations predict higher levels of turbulent transport in the third (highest TKE) and second (higher TKE) planes than the first plane near the endwall. Figure 7 present the magnitudes of local vorticity in the first three planes. The near wall vorticity

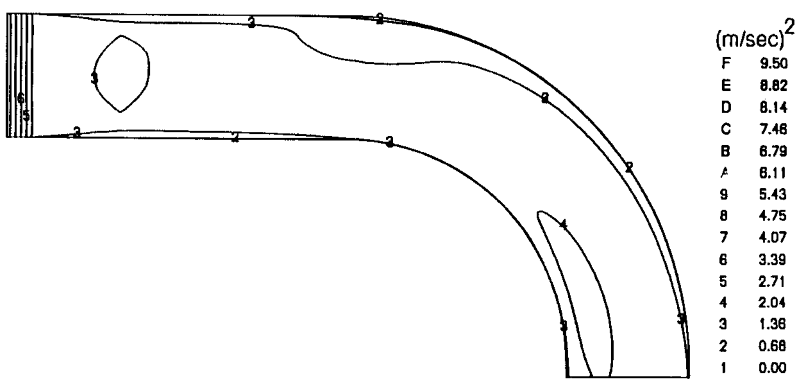

FIGURE 6a TKE at the first grid point away from the end-wall.

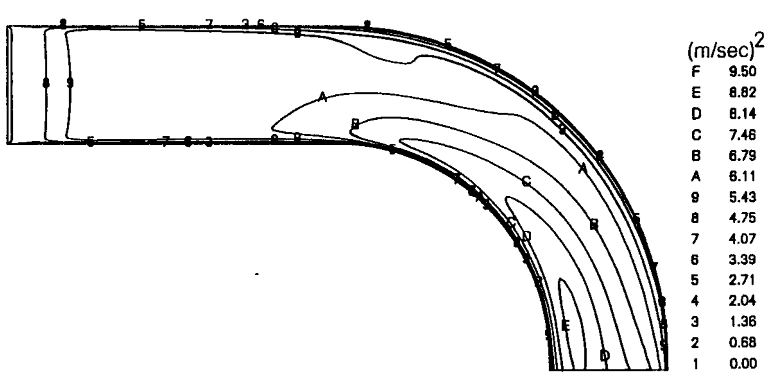

FIGURE 6b TKE at the second grid point away from the end-wall.

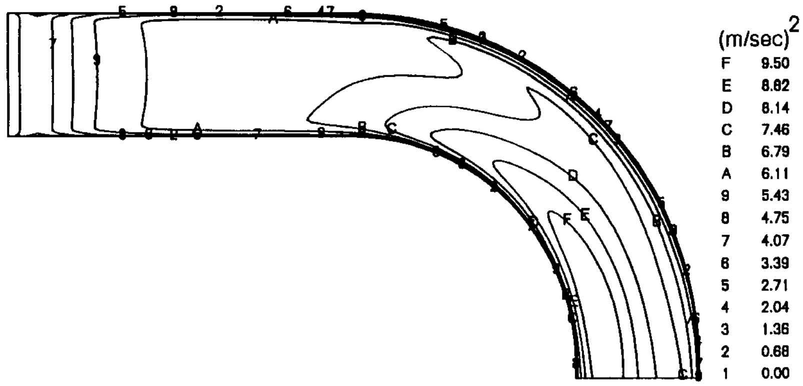

FIGURE 6c TKE at the third grid point away from the end-wall.

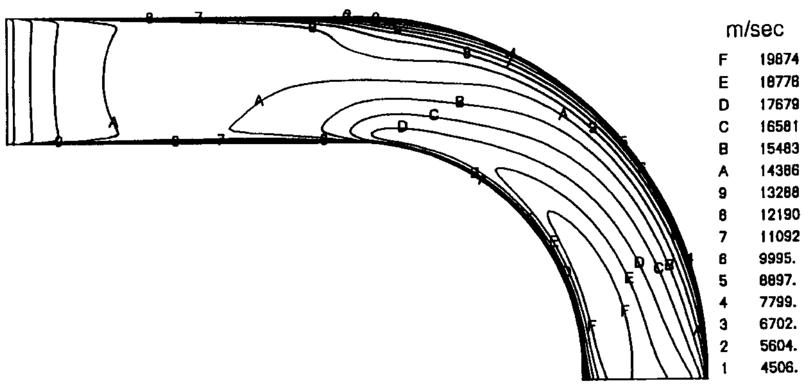

FIGURE 7a Vorticity at the first grid point away from the end-wall.

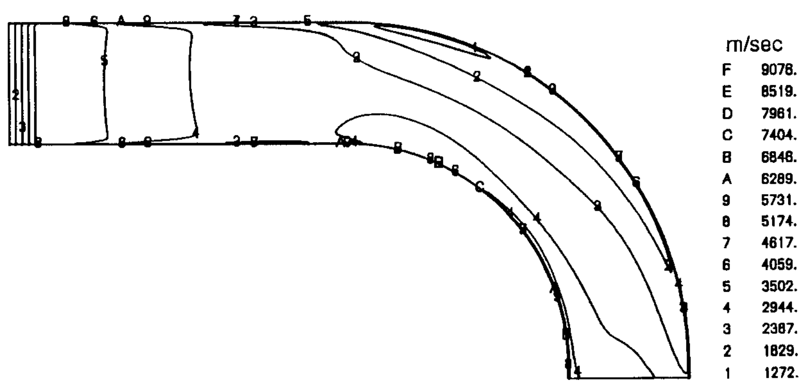

FIGURE 7b Vorticity at the second grid point away from the end-wall.

distributions are also qualitatively similar to TKE and heat transfer coefficient distributions. These results show that the local TKE level and the endwall vorticity significantly affect the endwall heat transfer behavior.

Computational simulations shown in Figure 6 indicate a high TKE region near the inlet section of the duct. It should be noted that the conduction heat loss through the sidewalls could also result in a slight increase in the uncertainty of the heat transfer coefficient in this region. Steep gradients in the heat transfer coefficient along the outer radius surface (*C*) within the 90° bend are visible. The passage vortex may produce significant vorticity near the outer and inner radii corner regions. The cross-stream velocities that indicate strong vorticity content in these regions are clearly shown in

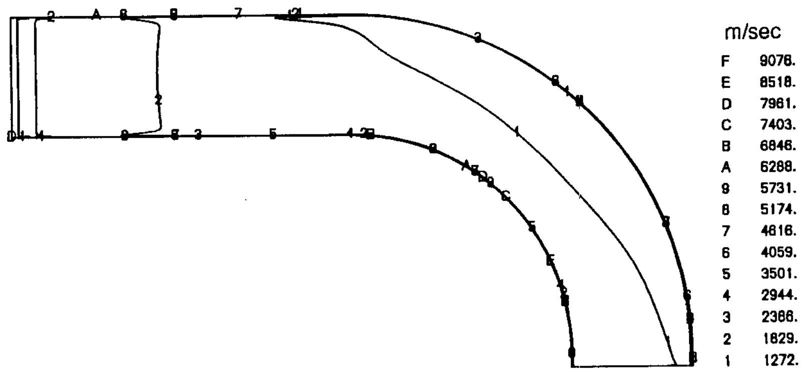

FIGURE 7c Vorticity at the third grid point away from the end-wall.

detailed measured hydrodynamic data presented in Wiedner (1994). Vorticity augmentation is much more significant near the inner radius corner than near the outer radius corner. The augmentation of the magnitude of the mean vorticity vector near the inner radius corner is also shown from measurements and computations, in Figure 7 of Part I. Current computations were capable of showing the direct relationship between heat transfer coefficient (Figure 4), TKE (Figure 6) and vorticity magnitude (Figure 7). Figures 6 and 7 indicate that the computed mean vorticity magnitude coincides with the regions of enhanced turbulent flow activity. The points on the endwall surface under the influence of these high TKE regions could experience enhanced turbulent heat transport from the endwall. The highest heat transfer rates are at the entrance section of the straight section of the duct and near the convex side of the endwall surface that is exposed to the passage vortex system.

Comparison of measured heat transfer coefficients with numerical computations showed about 10% to 20% underprediction on the heated endwall surface. Using a wall function approach may not be the most accurate method of resolving the fluid mechanics and heat transfer characteristics of near wall regions. However, the use of wall functions is a useful approximation that reduces the overall time consumption of the computation. This approach also eliminates the need for an extremely fine computational grid that may not be practical for the current viscous flow calculations. Computational results sufficiently simulate the general features of the measured heat transfer coefficients on the endwall surface. The characteristic wedge shape (Path I) observed in the measured heat transfer distribution is fully simulated by the computations as shown in Figure 4a. The heat transfer influence of the secondary flows as indicated by region (G) of measurements is also recovered in the numerical simulations. The contour levels 8, 9, A and B of the computed distribution as shown in Figure 4a are clearly visible in the measured distribution presented Figure 4b.

Independence of h from Thermal Boundary Conditions

In forced convection heat transfer, the heat transfer coefficient h is defined as a hydrodynamic indicator that should be independent of thermal boundary conditions. As long as the local Reynolds number distribution in the flow is preserved, variations in wall temperature or in free stream temperature does not influence the magnitude of h. The endwall heating rate can be easily changed by varying the applied voltage to the electrical bus bars located along line AB and CD. Two different endwall heating schemes resulted in very similar heat transfer coefficient distributions confirming the idea that local wall heat flux in forced convection problems is linearly dependent on the temperature difference between the free stream and the wall. This idea is closely related to the fact that momentum and thermal energy equations are not coupled in incompressible flow.

Temperature Distribution in the Passage

The influence of secondary flows on local temperature distributions in a 90° turning duct can be numerically visualized for the current conditions with a uniform inlet temperature of 289°K. The local thermal energy released from the top endwall surface is mainly distributed in the duct by forced convection, molecular and turbulent diffusion of heat and viscous dissipation. The resulting temperature distributions in 0°, 45°, and 90° cross sections are given in Figure 8.

At 0°, the temperature distribution appears to be symmetric about the plane $Y/D = 0.5$ and upstream effect of the bend is little. Recall that on the top wall, the temperature distribution is not uniform as shown in Figure 3. The steep gradients can only be seen in the near-wall region where pure conduction process exists. At 45°, the fluid particles absorb more heat from the top wall and the secondary flow motion convects most of the thermal energy produced near the endwall to the inner

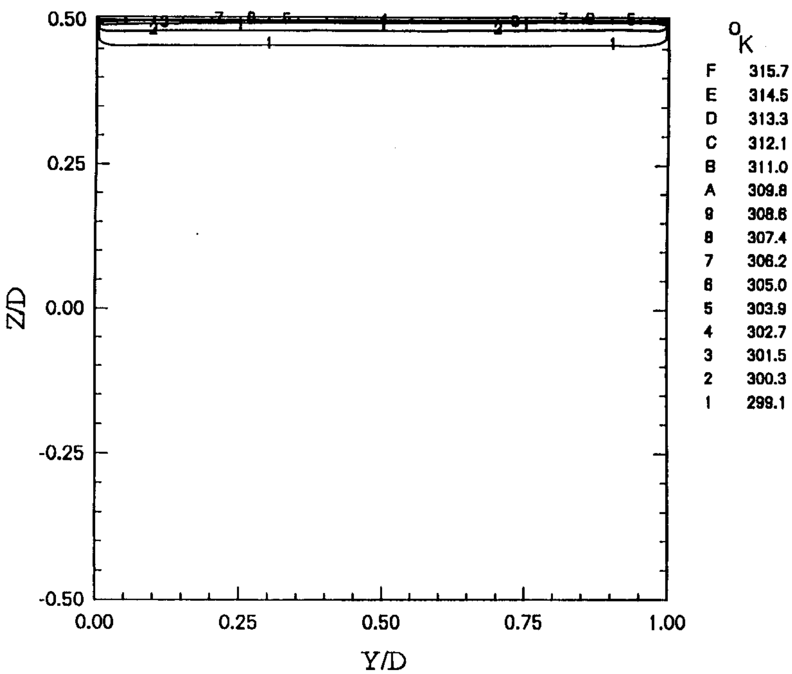

FIGURE 8a Temperature distribution at $X = 0°$.

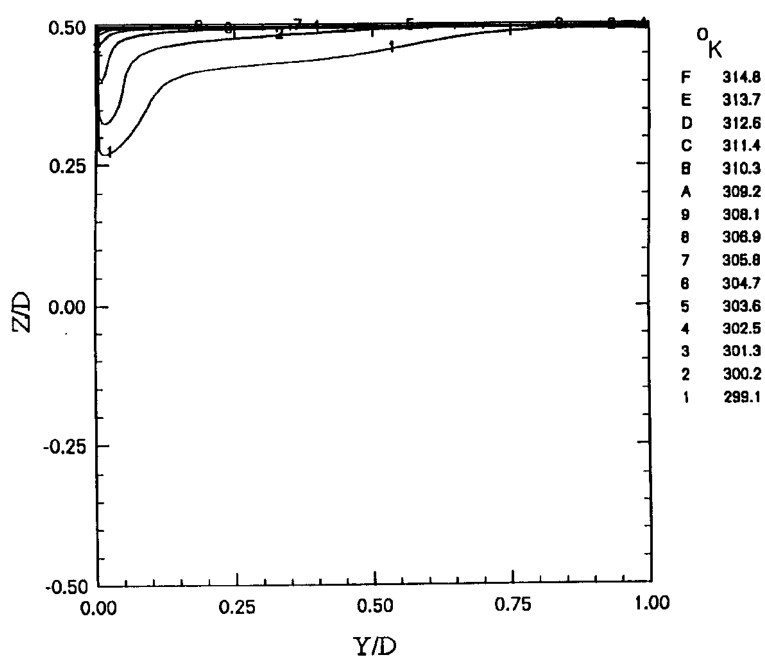

FIGURE 8b Temperature distribution at $X = 45°$.

wall. The cross flows on the endwall surface and the passage vortex clearly bring more thermal energy into the core of passage vortex from the top endwall surface as shown in Figure 8b. This phenomenon repeats itself in a stronger fashion as one moves from 45° section to 90° section in the streamwise direction. Contour line 1 is the boundary between the thermally undisturbed core flow zone (298°K) and the thermally contaminated zone. Figure 8c indicates the area coverage of the heated zone in the duct. The influence of the endwall heating can be felt in a non-negligible fashion even at the symmetry plane of the duct near $Z/D = 0$. It can be concluded from Figure 8

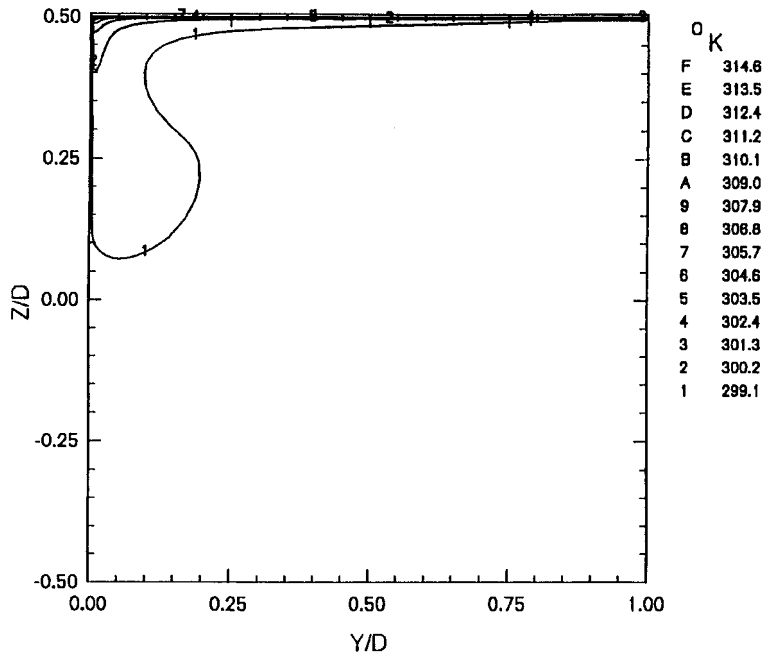

FIGURE 8c Temperature distribution at $X = 90°$.

that cross flows and secondary vortices can transport mass, momentum and heat from the concave part of the endwall to the convex end at a significant rate. Due to the highly rotational character of the flow near the convex surface, the transport mechanism is not limited to near endwall region.

Comparison of Molecular and Turbulent Heat Diffusion in the Passage

A comparison of molecular and turbulent heat flux components in the cross-stream plane of 90° section is presented in Figure 9. The distinction between the

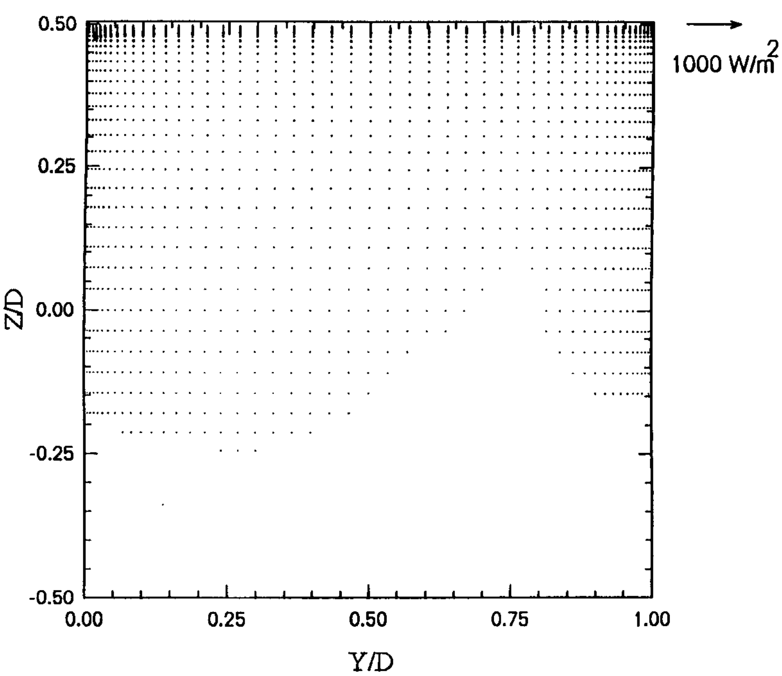

FIGURE 9a Molecular heat flux vector at $X = 90°$ (only cross-stream components).

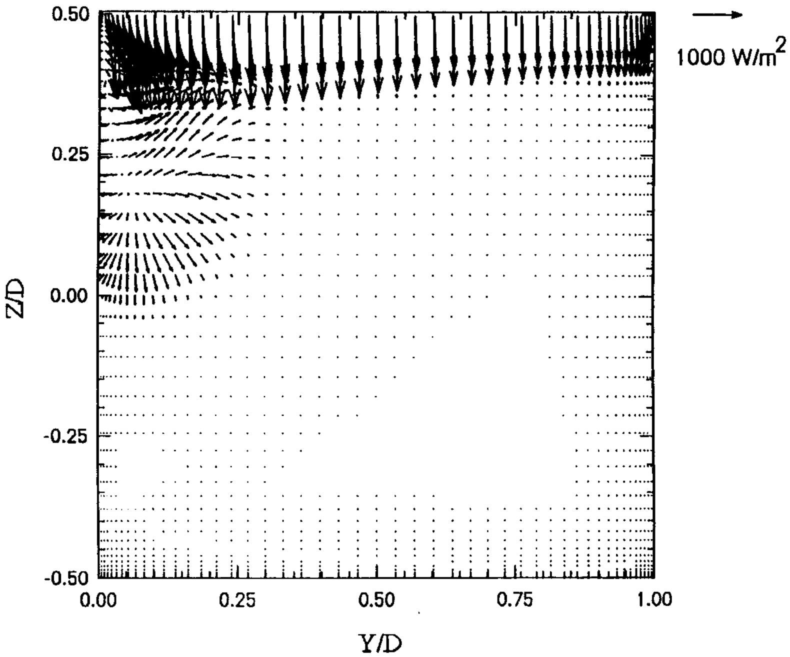

FIGURE 9b Turbulent heat flux vector at $X = 90°$ (only cross-stream components).

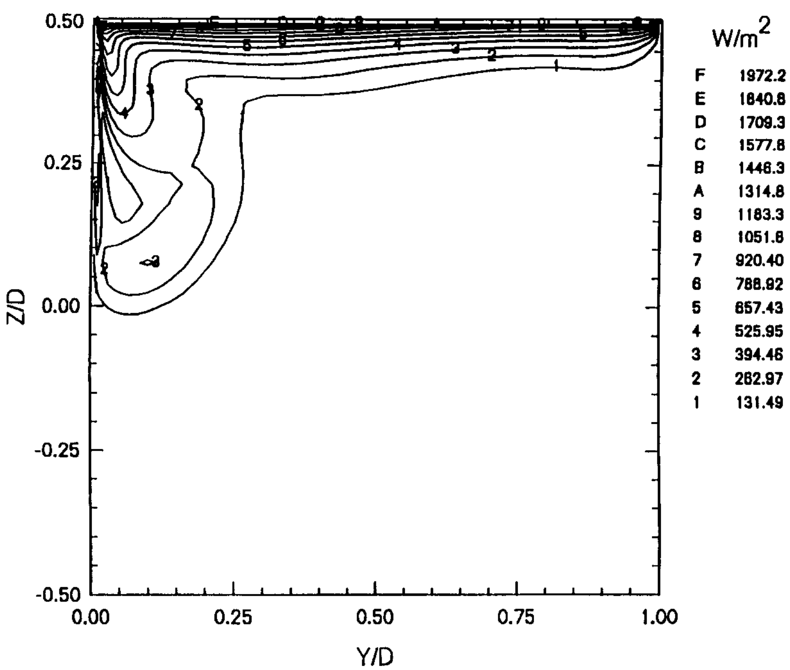

FIGURE 9c Magnitude of turbulent heat flux vector at $X = 90°$ (only cross-stream components).

molecular and turbulent diffusion process can be made by numerically evaluating the individual terms in thermal energy equation. A comparison of the two components suggests that most of the removal of thermal energy released from the endwall surface is achieved by the turbulent diffusion process. Strong turbulent heat flux vector components near the endwall as shown in Figure 9b are also apparent in the region where passage vortex dominates. The turbulent heat flux vectors become increasingly larger when one moves away from the core

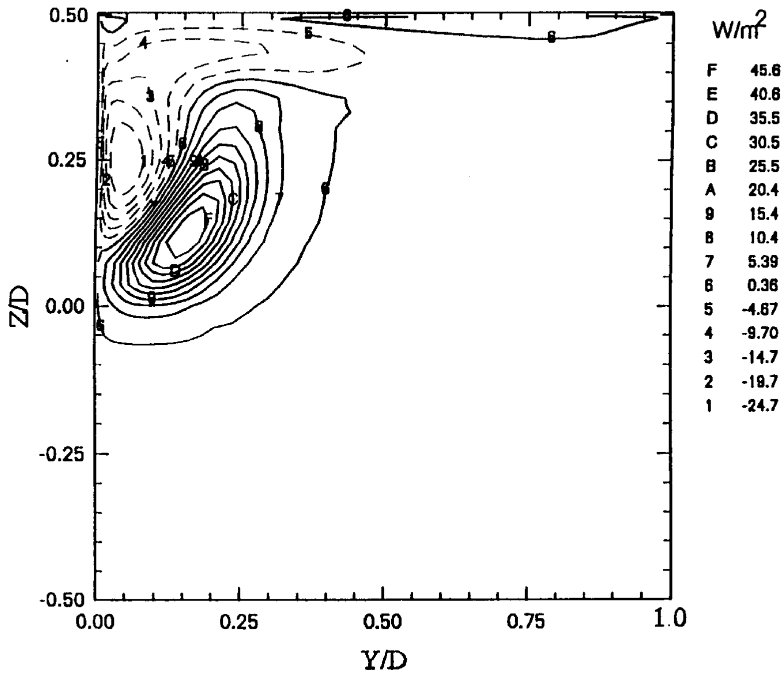

FIGURE 9d Total (molecular and turbulent) heat flux at $X = 90°$ (only streamwise component).

of the passage vortex. This region may be viewed as a flow zone rearranging the thermal energy distribution in a significant manner because of the existence of the passage vortex system. The contour plot of the magnitude of the turbulent heat flux vector is given in Figure 9c. Endwall cross flow and passage vortex influence on turbulent transport of heat clearly marked. Figure 9c suggests that the highest levels of turbulent heat transfer may appear near the passage vortex core, in addition to the near endwall region.

The magnitude of total streamwise heat flux including molecular and turbulent diffusion components is plotted in Figure 9d. This approach is useful in showing what specific directions are more dominant in transferring heat by molecular and turbulent diffusion process. Two different heat flux zones are observed near the convex surface, i.e., positive and negative zones. The negative zone is caused by the position change of the core of the temperature contour, just like the position change of vortex center in the streamwise direction. Since the heat flux is a function of temperature difference, a negative heat flux may result from the decreasing temperature in the streamwise direction. Moreover, the magnitude of streamwise heat flux was much less than the cross-stream magnitude representing the secondary flow effect. This implied that most of the heat diffusion process in the flow passage was in the $Y-Z$ plane, not in the streamwise direction.

CONCLUDING REMARKS

Convective heat transfer near the endwall surface of a 90° turning duct has been studied by using experimental flow/heat transfer methods and an in-house developed computational viscous flow/heat transfer solver.

When the endwall boundary layer develops in the curved section of the duct, cross-stream components of the velocity vector are enhanced due to the generation of the passage vortex. The endwall boundary layer is also subject to streamwise curvature. The interaction of the endwall boundary layer with the inner and outer radius sidewall boundary layers creates complex local wall heating rate distributions near the corner regions.

Elevated levels of local heat transfer coefficients on the endwall coincide with the flow regions that have high levels of measured vorticity and secondary velocity magnitude. In general, the regions of low heat transfer were associated with the locations where local streamwise velocities are relatively low.

A strong similarity between the measured/computed heat transfer contours and the computed TKE distribution near the endwall surface was observed.

The near wall vorticity distributions are also qualitatively similar to TKE and heat transfer coefficient distributions. These results show that the local TKE level and the associated endwall vorticity significantly affect the endwall heat transfer behavior.

In general, the computed mean vorticity magnitude coincides with the regions of enhanced turbulent flow activity. The points on the endwall surface under the influence of these high TKE regions could experience enhanced turbulent heat transport from the endwall.

Computational simulations can display the general features of the measured heat transfer coefficients on the endwall surface. The characteristic wedge shape (Path I) observed in the measured heat transfer distribution is fully simulated by the computations shown in Figure 4a. The heat transfer influence of the secondary flows as indicated by region (G) of measurements is also recovered from the numerical simulations.

Although at 0°, the temperature distribution in the duct cross section appears to be symmetric about the plane $Y/D = 0.5$, at 45°, the fluid particles absorb more heat from the top wall. The cross flow on the endwall surface and the passage vortex clearly brings more thermal energy into the core of the passage vortex from the top end-wall surface.

Cross-flows and secondary vortices can transport mass, momentum and heat from the concave part of the endwall to the convex end of the endwall at a significant rate. Due to the highly rotational character of the flow near the convex surface, the transport mechanism is not limited to near endwall region.

The distinction between the molecular and turbulent diffusion process can be made by computationally evaluating the individual terms in the thermal energy equation. The turbulent diffusion process removes most of the thermal energy that is released from the endwall surface. The highest levels of turbulent heat transfer may appear near the passage vortex core, in addition to the near endwall region.

Most of the heat diffusion process in the flow passage was in the $Y-Z$ plane, not in the streamwise direction.

A successful interpretation of local heat transfer phenomena influenced by a highly three-dimensional vortical flow requires an extensive evaluation of the local turbulent flow characteristics.

The current numerical approach may not be as accurate as the experimental heat transfer measurements. However, many details of the turbulent heat transport process that can not be measured directly by experimental methods can be visualized by the specific computational method.

Observations of the influence of a strongly three-dimensional flow on the near wall flow/heat transfer structure are possible via numerical methods. A comparison of the molecular/turbulent heat diffusion in selected flow cross sections, surface distributions of wall shear stress, visualization of local turbulent activity are a few of the tasks that can be performed using a numerical approach in a relatively time efficient manner.

High-resolution experimental flow/heat transfer data presented in this paper form a high quality baseline set for future assessments of three-dimensional viscous flow and heat transfer solvers that may originate from new computational strategies and turbulence models.

NOMENCLATURE

A	van Driest's constant
C_p	specific heat at constant pressure
C_{cor}	percentage of generated heat flux removed by forced convection
D	duct width
E	log-law coefficient and also electric field
h	heat transfer coefficient, $h = q''_w/(T_w - T_\infty)$
$\vec{J}$	current density
k	turbulent kinetic energy (also TKE)
Pr	Prandtl number
Pr_t	turbulent Prandtl number
q''_w	wall heat flux
Re	Reynolds number, $Re = \rho UD/\mu$
T	temperature
τ_w	wall shear stress
U_x, U_y, U_z	mean velocities in x, y, z-directions
V	electric potential
X, Y, Z	streamwise, radial and spanwise directions
x, y, z	cartesian coordinates
y_p, y	distance away from the wall
y^+	non-dimensional wall coordinate $y^+ = \sqrt{\tau_w/\rho} \cdot y/\nu$
δ	heater foil thickness
ν	kinematic viscosity $\nu = \mu/\rho$
Γ	isotropic diffusion coefficient
κ	von Karman constant
μ	molecular viscosity
μ_t	turbulent viscosity
ξ, η, ζ	transformed curvilinear coordinates
ρ	fluid density
σ	electrical conductivity

Subscripts

p	first grid point away from the wall
w	wall

Superscripts

$+$	non-dimensionalized wall quantity

REFERENCES

Brundett, E. and Baines, W. D. (1964) The Production and Diffusion of Vorticity in Duct Flow, *Journal of Fluid Mechanics*, **19**, 375–381.

Boyle, R. J. and Russell, L. M. (1989) Experimental Determination of Stator Endwall Heat Transfer, *NASA TM-101419*.

Camci, C. (1985) Experimental and Theoretical Study of Film Cooling on a Gas Turbine Blade, Ph.D. Thesis, Von Karman Institute for Fluid Mechanics/Katholieke Universiteit Leuven, Belgium.

Eibeck, P. A. and Eaton, J. K. (1987) Heat Transfer Effects of a Longitudinal Vortex Embedded in a Turbulent Boundary Layer, *ASME Journal of Heat Transfer*, **109**, 16–24.

Emery, A. F., Neighbors, P. K. and Gessner, F. B. (1980) The Numerical Prediction of Developing Turbulent Flow and Heat Transfer in Square Duct, *ASME Journal of Heat Transfer*, **102**, 51–57.

Gaugler, R. E. and Russell, L. M. (1984) Comparison of Visualized Turbine Endwall Secondary Flows and Measured Heat Transfer Patterns, *ASME Journal of Engineering for Gas Turbines and Power*, **106**, 168–172.

Gessner, F. B. (1973) The Origin of Secondary Flow in Turbulent Flow Along a Corner, *Journal of Fluid Mechanics*, **58**, 1–25.

Goldstein, R. J. and Spores, R. A. (1988) Turbulent Transport on the Endwall in the Region Between Adjacent Turbine Blades, *ASME Journal of Heat Transfer*, **110**, 862–869.

Graziani, R. A., Blair, M. F., Taylor, J. R. and Mayle, R. E. (1980) An Experimental Study of Endwall and Airfoil Surface Heat Transfer in a Large Scale Turbine Blade Cascade, *ASME Journal of Engineering for Power*, **102**, 257–267.

Johnson, R. W. and Launder, B. E. (1985) Local Nusselt Number and Temperature Field in Turbulent Flow Throughout a Heated Square-Sectioned U-Bend, *International Journal of Heat and Fluid Flow*, **6**, 171–180.

Kline, S. J. and McClintock, F. A. (1953) Describing Uncertainties in Single Sample Experiments, *Mechanical Engineering*, **75**, 3–8.

Launder, B. E. and Spalding, D. B. (1974) The Numerical Computation of Turbulent Flows, *Comp. Meth. Appl. Mech. Eng.*, **3**, 269–289.

Launder, B. E. and Ying, W. M. (1972) Secondary Flows in Ducts of Square Cross-section, *Journal of Fluid Mechanics*, **54**, 289–295.

Launder, B. E. and Ying, W. M. (1973) Prediction of Flow and Heat Transfer in Ducts of Square Cross Section, *Heat and Fluid Flow*, **3**, 115–121.

Mayle, R. E., Blair, M. F. and Kopper, F. C. (1979) Turbulent Boundary Layer Heat Transfer on Curved Surfaces, *ASME Journal of Heat Transfer*, **101**(3), 521–523.

Melling, A. and Whitelaw, J. H. (1976) Turbulent Flow in a Rectangular Duct, *Journal of Fluid Mechanics*, **78**, 289–315.

Myong, H. K. (1991) Numerical Investigation of Fully Developed Turbulent Fluid Flow and Heat Transfer in a Square Duct, *Journal of Heat and Fluid Flow*, **12**(4), 344–352.

Mori, Y., Uchida, Y. and Ukon, T. (1971) Forced Convective Heat Transfer in a Curved Channel with a Square Cross Section, *International Journal of Heat and Mass Transfer*, **14**, 1787–1805.

Perkins, H. J. (1970) The Formation of Streamwise Vorticity in Turbulent Flow, *Journal of Fluid Mechanics*, **44**, 721–738.

Wiedner, B. G. (1994) Passage Flow Structure and Its Influence on Endwall Heat Transfer in a 90° Turning Duct, Ph.D. Thesis, The Pennsylvania State University.

Wiedner, B. G. and Camci, C. (1996) Determination of Convective Heat Flux on Heat Transfer Surfaces with Arbitrarily Specified Boundaries, *ASME Journal of Heat Transfer*, **118**(4), 1–8.

Wiedner, B. G. and Camci, C. (1996) Passage Flow Structure and its Influence on Endwall Heat Transfer in a 90° Turning Duct: *Turbulent Stresses and Turbulent Kinetic Energy Production*, *ASME paper 96-GT-251*, International Gas Turbine Congress, Birmingham, UK.

Wiedner, B. G. and Camci, C. (1997) Passage Flow Structure and Its Influence on Endwall Heat Transfer in a 90° Turning Duct: *Mean Flow and High Resolution Endwall Heat Transfer Experiments*, *ASME Journal of Turbomachinery*, **119**(1), 39–50.